Icarus 367 (2021) 114542

Contents lists available at ScienceDirect

Icarus

journal homepage: www.elsevier.com/locate/icarus

Research Paper

Raman semi-quantification on Mars: ExoMars RLS system as a tool to better comprehend the geological evolution of martian crust

Marco Veneranda [a,*], Jose Antonio Manrique-Martinez [a], Clara Garcia-Prieto [a], Aurelio Sanz-Arranz [a], Jesús Saiz [a], Emmanuel Lalla [b], Menelaos Konstantinidis [b], Andoni Moral [c], Jesús Medina [a], Fernando Rull [a], Luis Miguel Nieto [a], Guillermo Lopez-Reyes [a]

[a] University of Valladolid, 47151 Valladolid, Spain
[b] Centre for Research in Earth and Space Science, York University, Canada
[c] Department of Space Programs, National Institute of Aerospace Technology (INTA), Spain

ARTICLE INFO

Keywords:
Raman spectroscopy
Semi-quantification
Chemometrics
Mars
ExoMars mission
RLS

ABSTRACT

This work presents the latest chemometric tools developed by the RLS science team to optimize the scientific outcome of the Raman system onboard the ExoMars 2022 rover. Feldspar, pyroxene and olivine samples were first analyzed through the RLS ExoMars Simulator to determine the spectroscopic indicators to be used for a proper discrimination of mineral phases on Mars. Being the main components of Martian basaltic rocks, lepidocrocite, augite and forsterite were then used as mineral proxies to prepare binary mixtures. By emulating the operational constraints of the RLS, Raman datasets gathered from laboratory mixtures were used to build external calibration curves. Providing excellent coefficients of determination (R^2 0.9942÷0.9997), binary curves were finally used to semi-quantify ternary mixtures of feldspar, pyroxene and olivine minerals. As Raman results are in good agreement with real concentration values, this work suggests the RLS could be effectively used to perform semi-quantitative mineralogical studies of the basaltic geological units found at Oxia Planum. As such, crucial information about the geological evolution of Martian Crust could be extrapolated. In light of the outstanding scientific impact this analytical method could have for the ExoMars mission, further methodological improvements to be discussed in a dedicated work are finally proposed.

1. Introduction

The main objective of the ESA/ExoMars mission is to assess if live ever took hold on Mars (Vago et al., 2018). To do so, the Rosalind Franklin rover will interrogate subsurface samples and rocky outcrops found at Oxia Planum. Here, multi-analytical investigation will serve to reconstruct the evolution of Mars' water/geochemical environment and to verify the potential preservation of biomarkers (Vago et al., 2017). The vast majority of the landing site is covered by a ≈ 50 m-thick layer of mixed phyllosilicates (well known as optimal biomarkers preservers (Fornaro et al., 2018a; Fornaro et al., 2018b)) whose deposition dates back to the water/rock interactions occurred during the Noachian period (3.9 Ga) (Carter et al., 2016; Quantin et al., 2016). Partially capping the clay rich unit, 10–20% of the landing site shows remains of lava flows deposited during the Early Amazonian era (2.6 Ga) (Carter et al., 2016). As attested by craters distribution analysis, this unit faced strong erosion processes resulting in the progressive exposure of the underlying unit (Quantin et al., 2016). The most recently exposed clays have been sheltered from the extreme environmental conditions of the surface (e.g. direct exposition to UV light and cosmic rays, high thermal gradients, etc) until 100 Ma ago, which significantly increases the chances to detect potentially preserved biomarkers (Quantin et al., 2016; Mandon et al., 2019; Quantin-Nataf et al., 2017).

In addition to the described geological units, Oxia Planum also provides feasible access to additional targets of high scientific interest. Besides the deltaic deposit enriched with hydrated silica detected at the margin of the ellipse (Quantin-Nataf et al., 2019), high-resolution images from HIRISE (Sefton-Nash et al., 2020) captured the presence of a high relief at the centre of the landing site. As reported elsewhere, this geological inconsistency can be interpreted as a crystalline basement's outcrop (older geological layer >4.0 Ga) emerging from the sedimented clays' unit (Pajola et al., 2017). Furthermore, the Noachian unit presents

* Corresponding author.
E-mail address: marco.veneranda.87@gmail.com (M. Veneranda).

https://doi.org/10.1016/j.icarus.2021.114542
Received 23 October 2020; Received in revised form 7 May 2021; Accepted 18 May 2021
Available online 24 May 2021

deep impact craters which ejected boulders provide easy access to the mineralogical study of older geological layers (Pajola et al., 2017). Together with the study of the Amazonian capping units -whose mineralogical composition still need to be disclosed- the spectroscopic analysis of the described boulders and outcrops could help disclosing critical information about the geological evolution of the region, and, in a broader perspective, about variations in the magmatic activity/crustal formation of Mars through ages.

Indeed, it is well known Martian igneous rocks experienced a systematic evolution with geological time (Ehlmann and Edwards, 2014). According to the compositional analysis of Mex/OMEGA orbital data, the mineralogical composition of Martian mafic regions has been constantly dominated by feldspar, pyroxene and olivine minerals. However, from Noachian to Amazonian ages, magmatic rocks at the surface of Mars displayed a clear transition towards higher concentrations of high calcium pyroxene (HCP) and olivine phases (Poulet et al., 2009). The observed transitions have been used as mineralogical constraints to build mathematical models that served to predicts the thermochemical evolution of the mantle and the crust formation history of the planet (Baratoux et al., 2013; Breuer and Moore, 2015; Grott et al., 2013; Morschhauser et al., 2011). Even though the in-depth laboratory study of SNC meteorites has been used as additional source of mineralogical and geochemical constraints (Ferdous et al., 2017; Mari and Verrino, 2016; Kizovski et al., 2019; Warren et al., 2004; Hamilton et al., 2003; McSween et al., 1996), the refinement of the proposed models pass through the use of analytical data gathered on Mars by exploration landers and rovers.

In this sense, VisNIR (MicrOmega (Bibring et al., 2017)) and Raman (RLS (Rull et al., 2017; Moral et al., 2019)) spectrometers onboard the ExoMars rover could be effectively used to compare the composition of Amazonian volcanic deposits with the described Noachian outcrops and boulders, thus adding novel clues about the mineralogical evolution of Martian igneous rocks. In detail, the sensitiveness of Raman spectroscopy towards the detection of feldspars, pyroxene and olivine phases is well acknowledged (Freeman et al., 2008; Wang et al., 2001; Mouri and Enami, 2008): By studying the position of secondary peaks, Raman spectrometers can be used to discriminate phases belonging to the same mineral group, thus highlighting potential elemental (e.g. the Mg/Fe ratio within the olivine solid solution series (Kuebler et al., 2006)) and structural (e.g. monoclinic and orthorhombic pyroxene (Wang et al., 2001)) differences.

Besides qualitative data, the RLS science team is verifying whether the multi point Raman investigation of powdered samples (which has been selected as nominal operational mode of the RLS during mission (Vago et al., 2017)) could be used to extrapolate semi-quantitative information about the main mineral phases of Martian rocks and soils. As such, preliminary analytical works are being performed by means of the RLS ExoMars Simulator, which is a Raman system providing spectra qualitatively comparable to those of the ExoMars flight model (RLS-FM) (Veneranda et al., 2020a; Veneranda et al., 2019a). As proved in recent works, by emulating the ExoMars operational mode and by using the same algorithms developed for the RLS-FM to autonomously operate on Mars, reliable semi-quantitative results from Martian analogues of low mineralogical complexity (2 major phases) are obtained (Lopez-Reyes et al., 2013).

Considering the critical impact the semi-quantitative analysis of unaltered Martian Igneous rocks could have in reconstructing the evolution of the Martian crust, this work seeks to assess if and how RLS data could be used for a reliable estimation of feldspar-pyroxene-olivine concentration ratio from Martian igneous rocks. Having in mind the potential application of the chemometric tools under development to the treatment of the Raman datasets gathered by the RLS on Mars, the present analytical study has been organized as follows. First, a Raman-based qualitative study of a wide collection of feldspar, pyroxene and olivine minerals, selected from the Analytical Database of Martian Minerals (ADaMM) (Veneranda et al., 2020b), was carried out by means of the RLS ExoMars Simulator. After selecting the optimal vibrational indicators, mineral proxies were used to create three sets of binary mixtures. By emulating the automatic operating mode of the RLS-FM system, mineral mixtures were characterized by the RLS ExoMars Simulator. The chemometric models the RLS science team is developing in the framework of the ExoMars mission were then applied to the obtained datasets to create dedicated calibration curves. The binary calibration curves were finally used to extrapolate the ternary concentration ratio (olivine-pyroxene-feldspar) of Martian igneous rock's simulants.

2. Materials and methods

2.1. ADaMM database

ADaMM is a novel database providing diffractometric (XRD) and spectroscopic (Raman, NIR, LIBS) data collected from a wide collection of pure mineral phases that have been detected on Mars by orbital and on-ground analytical systems, as well as identified in the laboratory through the study of Martian meteorites. ADaMM also includes additional phases that, according to the alteration processes occurred at the geologic timescale, are most likely to be present at the (sub)surface of Mars. One of the main characteristic of the ADaMM database is to provide spectroscopic data collected by contact and remote Raman systems (as the RLS ExoMars Simulator, the RLS spare model, SimulCam and the LabRam HR Evolution) emulating RLS, SuperCam and Sherloc systems. Furthermore, additional data have been collected by coupling the mentioned spectrometers to atmospheric and temperature chambers simulating Martian environmental conditions. As a whole, the ADaMM database aims to facilitate ExoMars and Mars 2020 science operation teams (and, in a broader extent, the scientific community) on the proper interpretation of Raman data soon gathered on Mars.

Since the present work seeks to assess the potential use of the ExoMars/RLS system for the semi-quantitative study of Martian igneous rocks, the RLS ExoMars Simulator was used to characterize and investigate the vibrational features provided by a set of mineral phases selected from the pyroxene, feldspar and olivine groups. The selected samples are listed in Table 1.

2.2. Samples preparation

As suggested by preliminary studies, the multi point analysis (between 20 and 39 spots per sample) the ExoMars/RLS will carry out on powdered Martian could serve to estimate the relative concentration ratio of binary mineral mixtures (Lopez-Reyes et al., 2013; Veneranda et al., 2020c; Veneranda et al., 2021). Adding a degree of complexity to the RLS dedicated-chemometric tools so far developed by the RLS science team, this work seeks to assess whether the RLS could be potentially used to perform semi-quantitative mineralogical studies of ternary sample mixtures through the use of binary calibration curves. To this aim, olivine-, pyroxene- and feldspar-representative minerals were crushed, sieved and mixed at different concentration ratios to obtain 3 sets of binary mixtures with a granulometry closely resembling the powders produced by the ExoMars Rover Crushing station. Considering the modern knowledge about Martian geology and mineral distribution, the optimal proxies were selected from the sample collection used to create the ADaMM spectral database.

The three set of binary mixtures created by mixing augite, labradorite and forsterite are presented in Table 2.

In addition to these, Martian Laboratory Simulants (MLS samples) were prepared and used as problem samples to test the reliability of the proposed semi-quantification method. For this purpose, feldspar-, pyroxene- and olivine-proxies were mixed to obtain the concentration ratios provided in Table 3.

Table 1
list of phases selected from the ADaMM mineral collection.

Feldspar			
Mineral Phase	Formula	Structure	Provenance
Albite	$NaAlSi_3O_8$	triclinic	Landsverk Quarry, Norway
Labradorite	$(Ca,Na)(Al,Si)_4O_8$ [An. 50–70%]	triclinic	Boulouris, St Raphael, France
Anorthite	$CaAl_2Si_2O_8$	triclinic	Loch Scridain Mull, UK
Orthoclase	$KAlSi_3O_8$	monoclinic	Kopriva, Kyustendil, Bulgaria
Microcline	$KAlSi_3O_8$	triclinic	Mount Malosa, Malawi

Pyroxene			
Mineral Phase	Formula	Structure	Provenance
Wollastonite	$CaSiO_3$	triclinic/ monoclinic	Val di Serra, Italy
Enstatite	$MgSiO_3$	orthorhombic	Nye County, Nevada, USA
Ferrosilite	$FeSiO_3$	orthorhombic	Vordereifel, Germany
Diopside	$CaMgSi_2O_6$	monoclinic	Malaga, Spain
Hedenbergite	$CaFeSi_2O_6$	monoclinic	Isle of Skye, UK
Augite	$(Ca,Fe,Mg)_2(AlSi)_2O_6$	monoclinic	Umba Valley region, Kenya

Olivine			
Mineral Phase	Formula	Structure	Provenance
Forsterite	Mg_2SiO_4	orthorhombic	Svalbard Islands, Norway
Fayalite	Fe_2SiO_4	orthorhombic	Danakil depression, Ethiopia
Tephroite	Mn_2SiO_4	orthorhombic	Wermland, Sweden

2.3. Analytical instruments

Raman analysis were carried out by the RLS ExoMars simulator. As reported elsewhere (Lopez-Reyes et al., 2013; Veneranda et al., 2019b; Veneranda et al., 2020a) this is the most reliable tool to effectively emulate the scientific outcome of the RLS flight model. The instrument, assembled at the University of Valladolid using commercial components, is composed of a BWN-532 excitation laser (B&WTek) emitting at 532 nm, a BTC162 high resolution TE Cooled CCD Array spectrometer (B&WTek) and an optical head with a long WD objective of 50×. Optical geometry, range of analysis (70–4200 cm^{-1}), working distance (≈ 15 mm), laser power output (20 mW), spectral resolution (6–10 cm^{-1}) and spot of analysis (≈ 50 μm) are closely resembling those of the RLS instrument. In addition to that, the RLS ExoMars Simulator integrates the same algorithms used by the RLS to autonomously operate on Mars, such as sequential analyses, autofocus, optimization of the signal to noise ratio by automatically selecting the best acquisition parameters (Lopez-Reyes and Rull Pérez, 2017). A custom developed software based on LabVIEW 2013 (National Instruments, EEUU) was used to collect Raman spectra in the range between 70 and 4200 cm^{-1}. Concerning the analysis of the ADaMM samples listed in Table 1, bulk materials were automatically investigated at 20 different spots each. Considering that, during nominal operational mode, the RLS onboard the Rosalind Franklin rover will perform 20 to 39 analysis in a single line per sample, 5 lines of 39 spots were run for each binary mixture (see Table 2).

Beside Raman studies, the mineralogical homogeneity of the selected proxies was evaluated by XRD analysis. To this end, a Discover D8 X-Ray Diffractometer (Bruker) composed of a Cu X-ray excitation source (wavelength 1.54 Å) and a LynxEye detector was used. After further crushing, fine-powdered samples (granulometry ≤150 μm) were analyzed by setting a scan range between 5 and 70° 2θ, a step increment in 2θ of 0.01 and a count time of 0.5 s per step. The obtained diffractograms were then interpreted using the XPowder 2004.04.71 software (Martin, 2004) and the PDF-4 database (Kabekkodu et al., 2002).

2.4. Data treatment and analysis

Knowing the quantum efficiency of CCD detectors varies with the wavelength (being the optimal value reached between 400 and 680 nm), the intensity of all spectra was corrected by dividing, for the same wavenumbers, the intensity of the sample spectrum by the intensity of a reference standard (amorphous zinc borate, $Zn_3B_6O_{12}{\cdot}3{,}5H_2O$) (Sanz-Arranz et al., 2017). Intensity-corrected Raman spectra were then submitted to cosmic rays' elimination, baseline correction and normalization (to 1). These tasks were performed through IDAT/SpectPro, a software developed by the RLS team to receive, decode, calibrate and verify the telemetries generated by the RLS on Mars (Lopez-Reyes et al., 2018).

After treatment, Raman data gathered from olivine-pyroxene (OP samples), olivine-feldspar (OF samples) and feldspar/pyroxene (FP samples) binary mixtures were used to build three calibration curves. Deepening in the refinement of the chemometric tools that are being developed by the RLS science team, external curves were generated by taking into account the intensity ratio between the main Raman peaks of

Table 3
Mineralogical composition of standard ternary mixtures used as problem samples.

Sample ID	Ternary proportion		
	Olivine (wt%)	Pyroxene (wt%)	Feldspar (wt%)
MLS1	37.9	35.4	26.7
MLS2	43.2	9.8	47.0
MLS3	16.5	33.8	49.7
MLS4	36.7	50.5	12.8
MLS5	35.0	11.8	53.2

Table 2
Mineralogical composition of standard binary mixtures used for the external calibration procedure.

Olivine/Pyroxene Mixtures			Olivine/Feldspar Mixtures			Feldspar/Pyroxene Mixtures		
Sample ID	Olivine (wt%)	Pyroxene (wt%)	Sample ID	Olivine (wt%)	Feldspar (wt%)	Sample ID	Feldspar (wt%)	Pyroxene (wt%)
OP 0	0.0	100.0	*OF 0*	0.0	100.0	*FP 0*	0.0	100.0
OP 5	5.0	95.0	*OF 5*	5.0	95.0	*FP 5*	5.0	95.0
OP 10	10.6	89.4	*OF 10*	10.2	89.8	*FP 10*	10.0	90.0
OP 25	24.9	75.1	*OF 25*	25.0	75.0	*FP 25*	25.0	75.0
OP 37.5	30.5	69.5	*OF 37.5*	37.6	62.4	*FP 37.5*	37.5	62.5
OP 50	50.0	50.0	*OF 50*	50.0	50.0	*FP 50*	50.0	50.0
OP 62.5	63.0	37.0	*OF 62.5*	62.6	37.4	*FP 62.5*	62.6	37.4
OP 75	74.8	25.2	*OF 75*	75.0	25.0	*FP 75*	75.0	25.0
OP 90	90.1	9.9	*OF 90*	89.8	10.2	*FP 90*	90.0	10.0
OP 95	95.0	5.0	*OF 95*	95.0	5.0	*FP 95*	95.0	5.0
OP 100	100.0	0.0	*OF 100*	100.0	0.0	*FP 100*	100.0	0.0

the considered mineral phases. The equation used for this purpose is the following:

$$r_a = \frac{1}{n}\cdot\sum_n \frac{I_a}{I_a + I_b};\ r_b = \frac{1}{n}\cdot\sum_n \frac{I_b}{I_a + I_b}$$

where r is the estimated proportion concentration indicator (related to the proportion through the calculated calibration curve), *a* and *b* are the two mineral phases composing the binary mixture, *n* is the number of spots per line and *I* is the peak intensity of the spectrum (without baseline) at a determined spot.

Three binary calibration curves were obtained to calculate the relative proportions among each pair of endmembers: olivine-feldspar (OF), olivine-pyroxene (OP) and feldspar-pyroxene (FP). The calibration curves uncertainty was estimated by calculating the standard deviation among the mean values of the 5 lines, with a confidence interval of 95% (±2σ). All the calculations were performed using MATLAB R2019a.

Afterwards, the concentration ratios obtained from the binary curves were used to calculate the ternary concentration ratio of MLS samples by using the following equations (deduced from $\%_{fld} + \%_{oli} + \%_{pyr} = 100$):

$$\%_{fld} = \frac{100}{R_{OF} + 1 + 1/R_{FP}}$$

$$\%_{pyr} = \frac{\%_{fld}}{R_{FP}}$$

$$\%_{oli} = \%_{pyr} * R_{OP}$$

where R_{OF} is the olivine-feldspar concentration ratio calculated from the OF calibration curves, R_{FP} is the feldspar-pyroxene concentration ratio from the FP curves, and R_{OP} is the olivine-pyroxene concentration ratio calculated from the OP curves.

3. Results

3.1. Raman qualitative analysis of ADaMM minerals

3.1.1. Feldspars

Feldspars are tectosilicates whose elemental composition can be inscribed inside a Na-Ca-K ternary diagram. Knowing of the miscibility gap between Ca and K, two solid solutions are possible: minerals with a chemical composition between Ca- and Na-rich endmembers are known as plagioclases, while minerals between K and Na are named alkali-feldspar.

As detailed elsewhere (Freeman et al., 2008), the vibrational modes of feldspars can be grouped in 4 different regions. Wavelengths below 200 cm^{-1} (here, region R1) display cage – shear Raman modes. O-T-O deformation & T-O-T lattice modes are constraint between 200 and 400 cm^{-1} (R2). The characteristic doublet of feldspar, which is due to the breathing modes of the four membered tetrahedral rings, can be found in R3 (400–550 cm^{-1}), while the region between 550 and 1150 cm^{-1} (R4) displays the deformation and vibrational stretching modes of the tetrahedra. Knowing that changes in the elemental composition of the mineral entails variations in the vibrational modes, the RLS ExoMars Simulator was used to analyse the endmembers of the ternary diagram.

As Ca-rich endmember ($CaAl_2Si_2O_8$), anorthite spectrum is characterized by a main doublet at 478 and 503 cm^{-1}, two peaks of medium intensity at 170 and 280 cm^{-1} and additional minor signals in R4 (Fig. 1). Compared to anorthite, the vibrational profile of albite ($NaAl_2Si_2O_8$) shows a higher complexity, being R1 characterized by 3 peaks of medium intensity (partially overlapping) at 162, 185 and 208 cm^{-1}. As additional fingerprint, the main peak of R2 is found at 290 cm^{-1} (10 cm^{-1} higher that the anorthite counterpart). Similarly, the second peak of the characteristic doublet is found at 508 cm^{-1}, while R4 is characterized by the presence of multiple peaks. As triclinic K-rich endmember, the main R1 peak of microcline ($KAl_2Si_2O_8$) appears a lower wavelength (151 cm^{-1}). On the contrary, the main peak in R2 is found at 285 cm^{-1} thus being in an intermediate position between anorthite and albite ones (280 and 290 cm^{-1} respectively). Regarding the R3 region, a greater distance is observed between the two main peaks (475 and 512 cm^{-1}), together with the detection of an additional signal of medium-low intensity around 454 cm^{-1}. Finally, position and intensity of the Raman signals detected in R4 is very similar to those observed in the spectrum of albite.

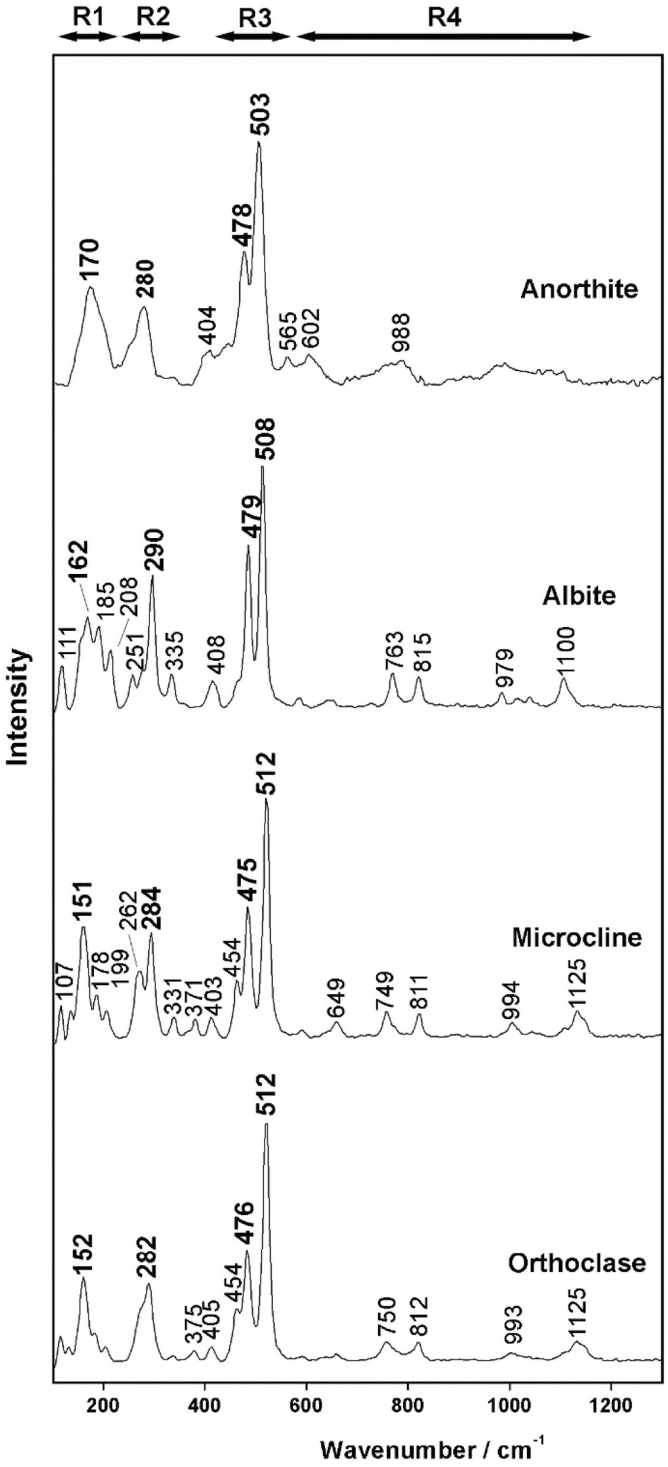

Fig. 1. Raman spectra collected by the RLS ExoMars Simulator from a selection of ADaMM feldspars' end-members.

Knowing the three endmembers have the same crystalline structure (triclinic) it follows that the variations in peak's position is mainly due to

the variation in their elemental composition. As displayed in Table 4, the RLS soon operating on Mars could be able to detect the shifting of the main peaks of feldspars detected in R1 (159 ± 9 cm^{-1}), R2 (284 ± 4 cm^{-1}) and R3 (517 ± 4 cm^{-1}) regions, thus providing information about the elemental composition of the mineral under analysis. Accordingly, the RLS team is working in the development of dedicated chemometric tools that, considering the main spectral features of endmembers, intermediate (from the two solid solutions) and ternary phases, could be used to optimize the discrimination of feldspars phases on Mars. In this regard, the Raman spectra of mineral polymorphs must also be taken into considerations. As such, Fig. 1 also displays the orthoclase ($KAl_2Si_2O_8$) spectrum, this being the monoclinic polymorph of the K-rich endmember. Compared to microcline, the degree of doublet shifting (482 and 521 cm^{-1}) is too low (between 0 and 2 cm^{-1}) to ensure a correct discrimination by RLS analysis. On the contrary, marked spectral differences can be found in R2. Here, microcline displays two clear signals of medium intensity at 262 and 284 cm^{-1}, while orthoclase provides a main peak at 282 cm^{-1} with a left shoulder resulting from the contribution of an additional minor signal at 276 cm^{-1}. Knowing that 1) spectral differences in R2 were observed in previous works (Freeman et al., 2008), and 2) intermediate phases polymorphs of the alkali solid solution series (e.g. monoclinic sanidine vs triclinic anorthoclase) display additional fingerprints between 200 and 400 cm^{-1} (Bendel and Schmidt, 2008), the detailed analysis of the spectral region R2 is expected to be of key importance to determine the crystal structure of feldspars on Mars.

3.1.2. Pyroxene

Within the inosilicate mineral group, the vibrational modes of pyroxene can be grouped in 4 main spectral regions. The stretching and bending modes of metal-oxygen bonds appears at wavelengths below 450 cm^{-1} (R1). From 450 to 600 cm^{-1} are the signals from O-Si-O bending modes (R2), while the strong Si—O bridging and non-bridging stretching modes are found in the wavelength ranges between 600 and 750 cm^{-1} (R3) and 850–1050 cm^{-1} (R4) respectively (Buzatu and Buzgar, 2010).

Even though Na-rich (e.g. eigirine $NaFe^{+3}Si_2O_6$ and jadeite $Na(Al, Fe^{3+})Si_2O_6$) and Li-rich (spedumene $LiAl(SiO_3)_2$) mineral species can be found, the majority of pyroxene minerals can be inscribed within a ternary diagram Ca-Fe-Mg. As most Ca-poor pyroxene, the orthorhombic crystalline structure of the Fe-rich endmember ferrosilite ($FeSiO_3$) emits a double peak in R4 (949 and 995 cm^{-1}). An additional strong signal is detected in region R3 (670 cm^{-1}, together with a medium signal at 654 cm^{-1}) while multiple strong (327 and 383 cm^{-1}) and medium/weak signals (224, 416, 513 and 530 cm^{-1}) are found below in R1 and R2. As Mg-rich endmember, enstatite ($MgSiO_3$) is also an orthorhombic mineral displaying a double peak in R3 (661 and 682 cm^{-1}). however, it can be differentiated from ferrosilite by an additional signal in region R4 that produces a right shoulder to the main peak found at 1009 cm^{-1}. This spectral feature combined with the position of R1 signals (above all, the main peak found at 341 cm^{-1}) can be used as Raman fingerprint of this mineral phase.

Fig. 2 also displays RLS ExoMars spectra of diopside ($CaMgSi_2O_6$) and hedenbergite ($CaFeSi_20_6$), these being the Mg- and Fe- endmembers of the respective solid solution. Compared to orthorhombic enstatite and

Table 4
Wavelength position and normalized intensity values of relevant Raman peaks from feldspar, pyroxene and olivine samples analyzed in this study.

Feldspar				Pyroxene				Olivine			
Mineral phase		Position (cm^{-1})	Intensity (norm.)	Mineral phase		Position (cm^{-1})	Intensity (norm.)	Mineral phase	Position (cm^{-1})	Intensity (norm.)	
Anorthite	Peak 1	170	0.48	Ferrosilite	Peak 1	328	0.73	Forsterite	Peak 1	822	1.00
	Peak 2	280	0.39		Peak 2	383	0.51		Peak 2	854	0.98
	Peak 3	484	0.58		Peak 3	670	0.57		Peak 3	917	0.04
	Peak 4	514	1.00		Peak 4	996	1.00		Peak 4	960	0.10
Albite	Peak 1	162	0.39	Enstatite	Peak 1	237	0.36	Fayalite	Peak 1	813	1.00
	Peak 2	290	0.56		Peak 2	343	0.50		Peak 2	837	0.80
	Peak 3	485	0.68		Peak 3	685	0.73		Peak 3	901	0.12
	Peak 4	513	1.00		Peak 4	1011	1.00		Peak 4	923	0.06
Microcline	Peak 1	151	0.48	Wollastonite	Peak 1	193	0.25	Tephroite	Peak 1	808	1.00
	Peak 2	284	0.46		Peak 2	412	0.27		Peak 2	840	1.00
	Peak 3	482	0.56		Peak 3	636	0.45		Peak 3	894	0.09
	Peak 4	519	1.00		Peak 4	970	1.00		Peak 4	932	0.05
Orthoclase	Peak 1	152	0.37	Diopside	Peak 1	322	0.54	**AVARAGE**	**Peak 1**	**814 ± 7.09**	**1.00 ± 0.00**
	Peak 2	282	0.34		Peak 2	390	0.61		**Peak 2**	**844 ± 9.07**	**0.93 ± 0.11**
	Peak 3	482	0.48		Peak 3	666	0.81		**Peak 3**	**904 ± 11.79**	**0.08 ± 0.04**
	Peak 4	521	1.00		Peak 4	1012	1.00		**Peak 4**	**938 ± 19.30**	**0.07 ± 0.03**
AVARAGE	**Peak 1**	**159 ± 9.00**	**0.43 ± 0.06**	Hedenbergite	Peak 1	305	0.37				
	Peak 2	**284 ± 4.32**	**0.44 ± 0.09**		Peak 2	373	0.55				
	Peak 3	**483 ± 1.50**	**0.51 ± 0.08**		Peak 3	659	0.77				
	Peak 4	**517 ± 3.86**	**1.0 ± 0.00**		Peak 4	1011	1.00				
				AVARAGE	**Peak 1**	**277 ± 59.30**	**0.45 ± 0.19**				
					Peak 2	**380 ± 25.25**	**0.49 ± 0.13**				
					Peak 3	**663 ± 17.94**	**0.67 ± 0.15**				
					Peak 4	**1000 ± 18.04**	**1.0 ± 0.00**				

Bold sections highlight the calculated average peak values

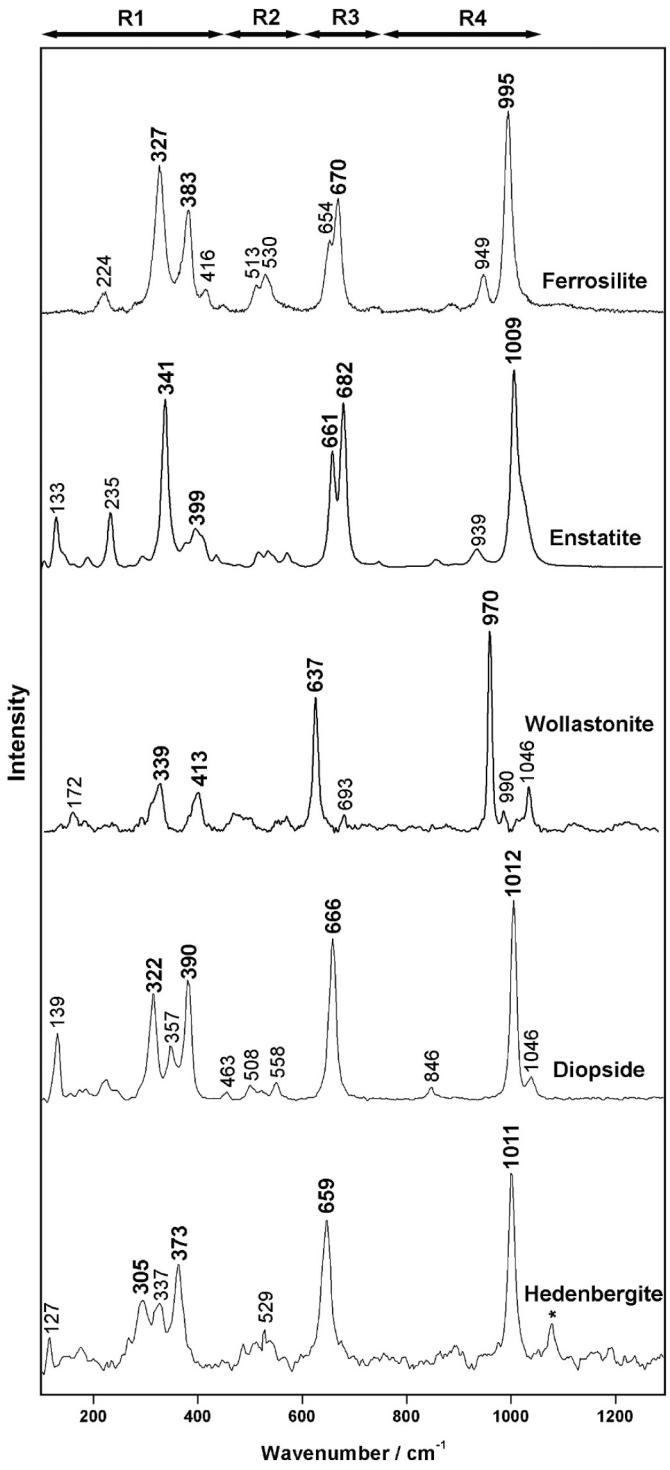

Fig. 2. Raman spectra collected by the RLS ExoMars Simulator from a selection of ADaMM pyroxene. * additional Raman signal proceeding from calcite impurities.

ferrosilite, these monoclinic phases provide two strong Raman peaks in regions R3 and R4, respectively: the shifting of the Si—O bridging stretching mode (at 666 cm^{-1} for diopside and 659 cm^{-1} for hedenbergite) can be effectively detected by the RLS system, while the Si—O non-bridging stretching one differs by only 1 cm^{-1} (at 1012 cm^{-1} for diopside and 1011 cm^{-1} for hedenbergite). Besides the position of the main R3 peak, the discrimination between the two endmembers can be optimized by analyzing the vibrational profile in the region below 450 cm^{-1} (R1). Here, both diopside (139, 322, 357 and 390 cm^{-1}) and hedenbergite (127, 305, 337 and 373 cm^{-1}) display 4 medium peaks which position and relative intensity varies markedly.

Finally, the RLS ExoMars Simulator spectrum of wollastonite (Ca-rich endmember) displays clear Raman signals at 172,339,413,637,693,970,990 and 1046 cm^{-1} (Fig. 2). In this case, the main peaks found at R3 and R4 appears at lower wavelengths (about 40 cm^{-1} of shifting) than others pyroxene phases. This spectroscopic feature greatly facilitates the discrimination of wollastonite from further phases (see Table 4).

Being in agreement with the main spectroscopic differences described above, the work of A. Wang et al. (Wang et al., 2001) confirms that stretching and bending modes of metal-oxygen bonds (below 450 cm^{-1}) are of key importance for a proper identification of pyroxene phases, especially for spectra collected by instruments with a spectral resolution between 6 and 10 cm^{-1} (as is the case of the RLS system). Beside mineral phase identification, the spectral features of pyroxene phases within the diopside-hedenbergite and enstatite-ferrosilite solid solutions vary according to the Mg/Fe concentration ratio (Huang et al., 2000). Under this assumption, through the development of dedicated chemometric tools, the Raman spectrometer onboard the Rosalind Franklin Rover may provide a rough estimation of the elemental composition of Martian pyroxene.

3.1.3. Olivine

Olivine are orthorhombic nesosilicates which general formula can be written as $M1M2SiO_4$, where M1 and M2 sites are occupied by ions such as Fe, Mg and Mn. Considering Mn concentration is generally below 1 wt % (Ishibashi et al., 2012), the chemical composition of olivine can be described almost entirely by the binary ratio Fe and Mg, thus placing most olivine minerals within the solid solution between forsterite (Fo, Mg_2SiO_4) and fayalite (Fa, Fe_2SiO_4) endmembers.

Since 1970, several scientific articles focused on the detailed spectroscopic characterization of forsterite and fayalite minerals (Servoin and Piriou, 1973; Devarajan and Funck, 1975). Regarding Raman spectroscopy, both compounds present 36 Raman active vibrations, which can be divided into three main groups (Ishibashi et al., 2008). Low and medium intensity peaks below 450 cm^{-1} (R1) are produced by lattice vibration modes (rotational and translational motions of SiO_4 as unit). Medium intensity peaks from 450 to 700 cm^{-1} (R2) are due to the internal bending vibration modes of SiO_4, while medium and high intensity peaks (R3) between 700 and 1100 cm^{-1} are produced by the internal stretching vibration modes of SiO_4.

As can be seen in Fig. 3, the RLS ExoMars Simulator spectrum of forsterite (Svalbard, Norway) displays the characteristic double peak at 822 and 854 cm^{-1}. In the same region, additional peaks of medium intensity are also detected at 917 and 960 cm^{-1}. With regards to lattice vibration modes, minor signals are observed at 192 (broad band), 300, and 428 cm^{-1} while two weak peaks are found in R2 (541 and 605 cm^{-1}). Compared to forsterite, the characteristic doublet of fayalite shifts towards lower wavelength, being the maximum intensities detected at 813 and 837 cm^{-1}. The magnitude of their shifting (9 and 17 cm^{-1}, respectively) makes the Mg- and Fe- endmembers to be easily distinguished by the RLS. In addition to that, the vibrational profile within R1 and R2 regions is also different (main peaks detected at 170, 236, 288, 382, 508 and 562 cm^{-1}). As explained elsewhere, being the vibration mostly affected by changes in cation volume and mass, peaks assigned to M2 translation (from 300 to 390 cm^{-1}) show the greatest variation with composition (Chopelas, 1991). Having a solid solution between forsterite and fayalite, changes in the Fe/Mg ratio implies variations in both intensity and position of Raman vibrational modes. Accordingly, the wavelength shifts of the main doublet around 820 and 850 cm^{-1} has been deeply studied with the purpose of formulating empiric equations that, from Raman spectra interpretation, enable to estimate the Fo–Fa composition of olivine crystals (Mouri and Enami, 2008; Kuebler et al., 2006; Torre-Fdez et al., 2017). Taking into account

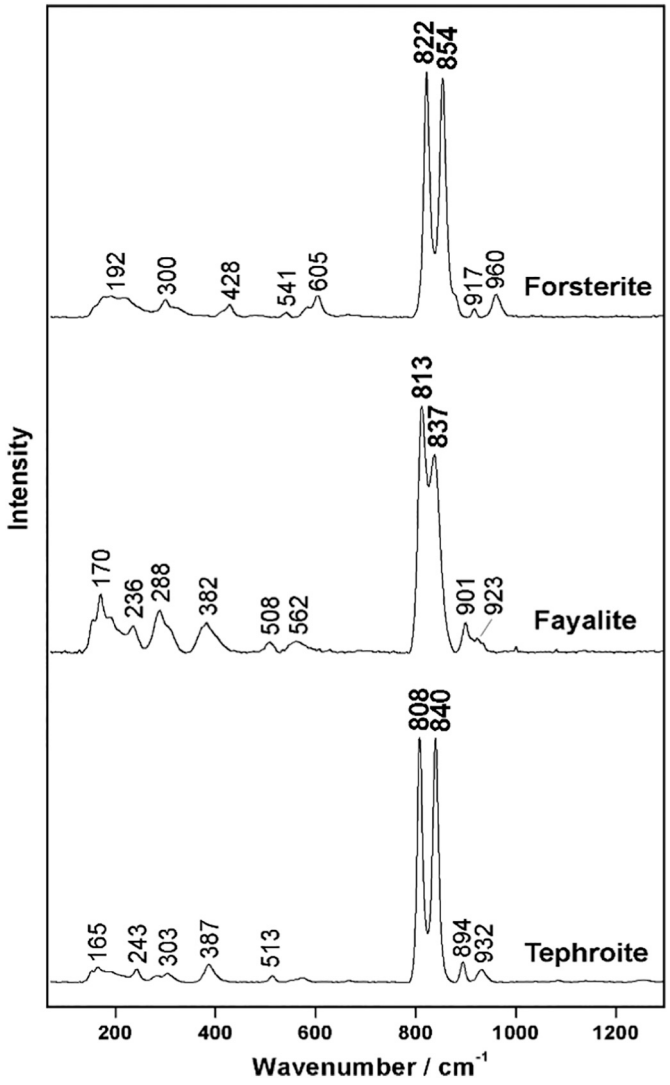

Fig. 3. Raman spectra collected by the RLS ExoMars Simulator from a selection of ADaMM olivine.

the possible errors derived from the lower spectral resolution of Raman flight models, the RLS team is developing dedicated calibration curve that optimizes the estimation of the Fo/Fa ratio by taking into account (beside the main doublet) the additional information provided by the displacement of secondary peaks (see Table 4).

Even though Mn is often found as minor addition (below 1 wt%), Mg-rich olivine can be rarely found on Earth. As displayed in Fig. 3, the tephroite sample from Wermland (Sweden) displays a further shifting of both main peaks (808 and 840 cm^{-1}), while additional minor signals are found at 165, 243, 303, 387, 513, 894 and 932 cm^{-1}. Knowing that Mn can replace both structural Fe and Mg ions, two additional solid solutions with forsterite and fayalite are possible. However, due to the scarcity of available natural samples, no semi-quantification Raman model has been presented to date.

Beside spectra comparison, Raman data gathered by RLS ExoMars simulator were treated using the SpectPro/IDAT software as described in section 2.4. Wavelength position and normalized intensity values of the main Raman peaks detected from the analyzed phases are reported in Table 4.

3.2. *Raman-XRD analysis of the selected pyroxene-, feldspar- and olivine-proxies*

Plagioclases are well known for being the most abundant mineral phases at the Martian surface (Riu et al., 2019). Recently, the linear deconvolution of Thermal Emission Spectrometer (TES) spectra has been carried out to determine chemical variabilities within the group. As the resulting compositional map proved that Mars is dominated by calcic plagioclase having an average composition of An61 (Milam et al., 2010), a labradorite sample from Boulouris (France) was selected as proxy of this mineral group. As can be seen in Fig. 4, the Raman spectrum gathered from the selected sample displays clear vibrational peaks whose position (180, 282, 479, 509, 562, 604 cm^{-1}) fit with those provided by labradorite minerals patterns presented elsewhere (Freeman et al., 2008; Lafuente et al., 2015).

Together with plagioclase, pyroxene minerals dominate the mineralogy of Martian crust. A detailed overview of global pyroxene distribution on Mars and its compositional diversity have been gathered by OMEGA remote observations (Mustard et al., 2005), which identified an higher abundance of high-calcium pyroxene phases (HCP) over low-calcium ones (LCP) (Rogers and Christensen, 2007). Considering that, as demonstrated by Raman-based laboratory studies, augite is often found as main HCP mineral of Martian meteorites (Hu et al., 2011; Treiman, 2005), augite crystals from the Umba Valley region (Kenya) were used as pyroxene proxy. As displayed below, the Raman spectrum of the selected mineral provides medium to strong peaks at 132, 327, 392, 667 and 1006 cm^{-1} that fit with reference spectra provided elsewhere (Fig. 4) (Buzatu and Buzgar, 2010).

Unlike Mars, where olivine crystals tend towards the endmember fayalite (Koeppen and Hamilton, 2008), Fe-rich minerals are rarely found on Earth (average composition is $Fo_{86}Fa_{12}$ (Kolesov and Geiger, 2004)). Knowing that ADaMM fayalite samples are too small to prepare multiple sets of mineral mixtures, a Mg-rich mineral samples was used as olivine proxy. As can be seen in Fig. 4, the RLS ExoMars Simulator spectrum obtained from the selected mineral (from Svalbard's islands, Norway) displays a doublet at 822 and 854 cm^{-1} together with medium peaks at 918 and 960 cm^{-1} and several minor signals at wavelengths below 650 cm^{-1} (vibration regions R1 and R2).

Besides qualitative Raman analysis, the three selected mineral proxies where characterized by XRD to determine the potential presence of additional mineral phases that could negatively affect the construction of the calibration curves. As displayed in Fig. 5, the diffractograms gathered form the powdered materials only display the characteristic peaks of labradorite (main signals at 21.95, 24.40, 27.80, 28.85 and 51.40 2-theta (Huang and Gandais, 1985)) augite (29.85, 35.70, 42.40,

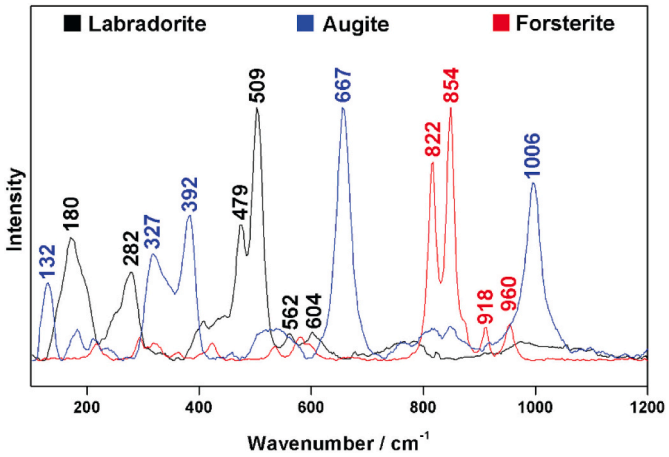

Fig. 4. RLS ExoMars Simulator' characteristic spectra of labradorite, augite and forsterite mineral samples, which were used in this work as plagioclase, pyroxene and olivine proxies.

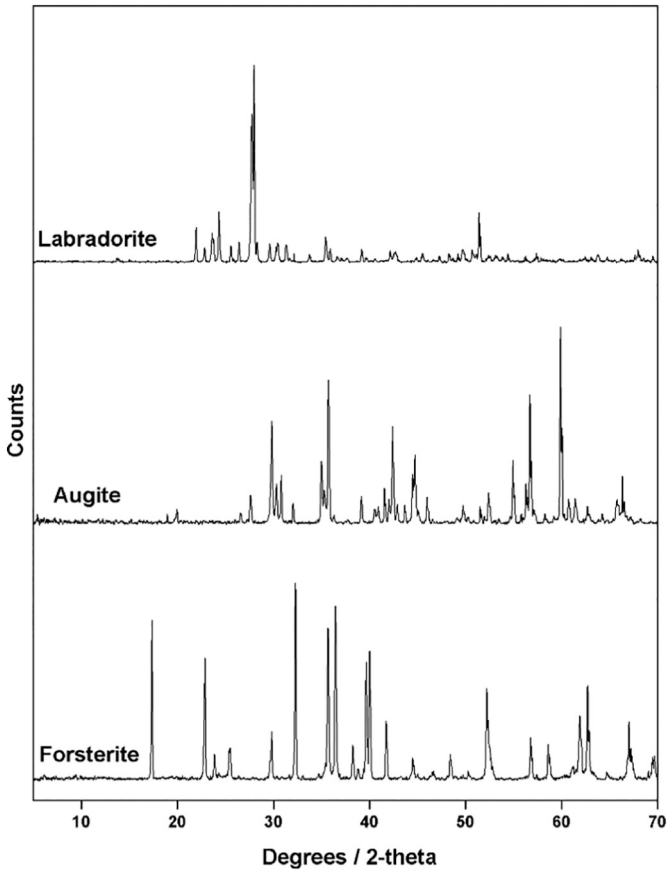

Fig. 5. Diffractogram of labradorite, augite and forsterite mineral samples used in this work as plagioclase, pyroxene and olivine proxies.

56.70 and 59.80 2-theta (Lafuente et al., 2015)) and forsterite (17.38, 32.35, 35.75, 36.55 and 40.10 2-theta (Lafuente et al., 2015)). Accordingly, impurities are either absent or below the detection limit of the instruments (around 5%, depending on the selected acquisition parameters and further variables).

3.3. Construction of PO, FO and FP calibration curves

Taking into account the intensity ratio between the main peak of each selected proxy, the binary mineral mixtures presented in section 2.2 were used to build external calibration curves. Spectroscopic indicators were selected by considering average peaks' intensity and by avoiding regions of potential signals overlapping. As shown in Fig. 4, the chosen vibrational modes (around 509 cm^{-1} for feldspars, 667 cm^{-1} for pyroxene, and 854 cm^{-1} for olivine) are the one providing the most intense Raman signal in the spectrum. Furthermore, as demonstrated by the spectral comparison provided in Fig. 4, no peak overlapping occurs within the selected regions, which minimizes potential semi-quantification errors. Knowing that the position of the selected vibrational mode may vary with the elemental composition and/or the crystal structure of the mineral phase, the chemometric model was designed to automatically detect, for each selected area, the maximum intensity value within a range of ± 10 cm^{-1}.

After peak selection, the relative concentration ratio of each binary mixture was calculated by averaging the intensity ratio obtained from each of the 39 points analyzed to build the Raman data-set, this being the maximum number of analysis the RLS will perform on Martian samples during nominal operation. The uncertainty was finally estimated within 95% confidence bounds by calculating two-times the standard deviation of the proportions gathered from the 5 line-datasets collected from each sample mixture.

The results obtained by analyzing the Raman datasets gathered from all binary mixtures are provided in Table S1.

By plotting the calculated intensity ratio (Y axis) versus the real proportion (wt-%, X axis) of the samples listed in Table 2, the calibration curves represented in Fig. 6 were obtained:

The equation describing the olivine-pyroxene calibration curves (OP samples) to calculate the proportion as a function of r_{oli} and r_{pyr} are:

$r_{oli} = -0.010154 \cdot prop_{oli}^2 + 0.040988 \cdot prop_{oli} + 97.412314$; $R^2 = 0.9997$

$r_{pyr} = 0.010154 \cdot prop_{pyr}^2 - 0.40988 \cdot prop_{pyr} + 2.587685$; $R^2 = 0.9997$

For the olivine-feldspar curves (OF samples):

$r_{oli} = -0.00480 \cdot prop_{oli}^2 - 0.59710 \cdot prop_{oli} + 102.20266$; $R^2 = 0.9942$

$r_{fld} = 0.00480 \cdot prop_{fld}^2 + 0.59710 \cdot prop_{fld} - 2.202266$; $R^2 = 0.9942$

And for the feldspar-pyroxene calibration curves (FP samples):

$r_{fld} = -0.00393 \cdot prop_{fld}^2 + 1.35420 \cdot prop_{fld} + 4.66349$; $R^2 = 0.9996$

$r_{pyr} = 0.00393 \cdot prop_{pyr}^2 - 1.35420 \cdot prop_{pyr} + 95.33651$; $R^2 = 0.9996$

Calculated as $\pm 2\sigma$, the maximum uncertainty of the measure is $\pm 6.3\%$ for OP mixtures, $\pm$ 8.9% for OF mixtures and $\pm$ 5.3% for FP mixtures.

3.4. Raman-based semi-quantitative analysis of ternary mineral mixtures

As in the case of binary mixtures, MLS samples were investigated with the RLS ExoMars Simulator by analyzing 5 lines of 39 points. Even though the RLS system will nominally perform one set of 39 Raman analysis on Martian powdered samples, five lines were here analyzed to provide a statistical reference of the expected uncertainty of the method. The results gathered by applying the proposed calibration curves are summarized in Table 5 together with the uncertainty value calculated with a 95% confidence bound (Binary concentration ratios). From the three sets of binary concentration ratios, the semi-quantification of feldspar-pyroxene-olivine content was extrapolated from MLS samples (Ternary estimation) by using the equation described in section 2.4. The difference between real concentration ratios (presented in Table 3) and estimated concentration of each mineral phase are also presented in Table 5 (Error).

The classification goodness of the proposed chemometric model was calculated by measuring the Euclidean distance (Ed) between real and Raman-estimated concentration values. To facilitate results interpretation, real and estimated concentrations ratios were plotted in a ternary diagram. In general, Raman semi-quantification results are in good agreement with real concentration values. Indeed, except for MLS2 (Ed = 12.8), the Euclidean distance measured in all problem samples goes from 3.35 to 8.11. As displayed in Fig. 7, the proposed chemometric model tends to underestimate the concentration of feldspar phases in the samples. This error seems to increase by increasing the olivine-pyroxene ratio, as is the case for MLS5. The vibrational profiles of untreated MLS5 and MLS2 spectra (samples having similar concentration ratios but different semi-quantification error) were compared: the sample providing the greatest Ed value is also the one showing the greatest variability (from spectrum to spectrum) in the intensity of the fluorescence background. In this regard, the RLS science team is planning a dedicated research to evaluate the factors affecting the fluorescence (e.g. granulometry) and the magnitude of their influence in the variation of Raman peaks intensities. To further optimize the reliability of Raman semi-quantification studies, the potential effects entailed by additional parameters (such as mineral crystallinity and acquisition parameters conditions, among others) will be also evaluated and presented in a dedicated manuscript, which must be interpreted as a continuation of the present work.

Fig. 7 also displays the ternary concentration ratios of real Martian rocks and soils, as they have been analyzed by Spirit (Gu1 = Basaltic soil,

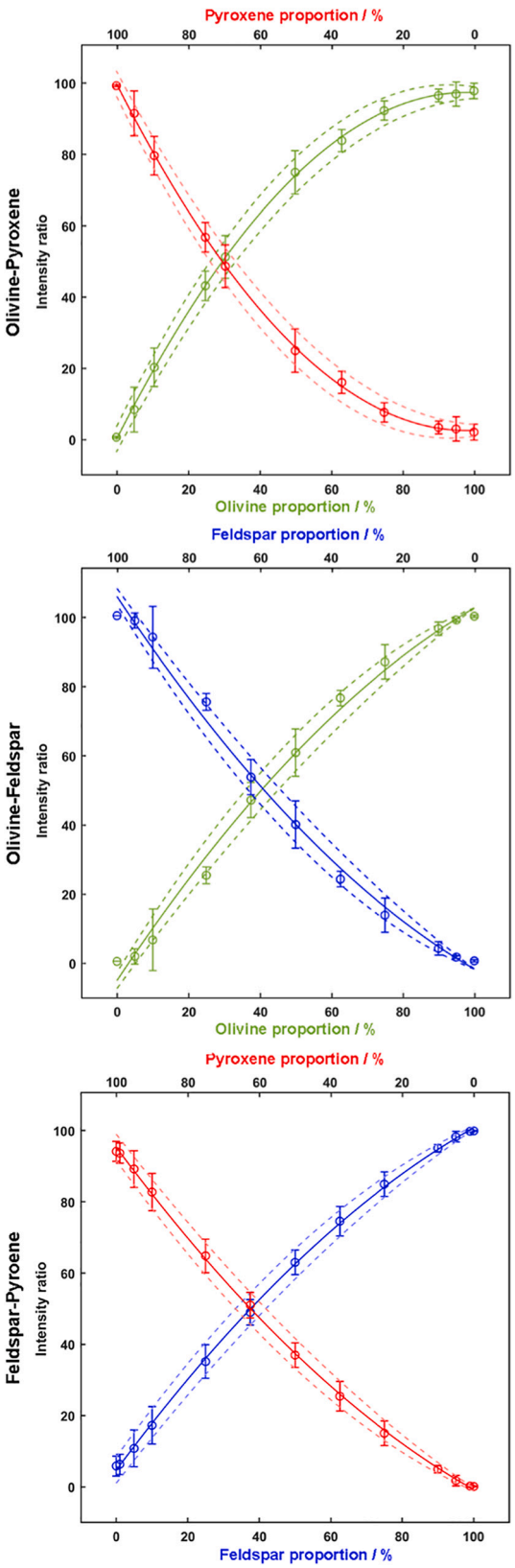

Fig. 6. OP, OF and FP calibration curves obtained by averaging the intensity ratio of RLS ExoMars Simulator datasets (5 * 39 points) gathered from binary mineral mixtures of known concentration.

Gu2 = Backstay, Gu3 = Adirondack and Gu4 = Algonquin (Poulet et al., 2009)) and Curiosity (Ga1 = Cumberland, Ga2 = Jhon Klein and Ga3 = Rocknest (Allan et al., 2016)) rovers operating at Gale and Gusev craters, respectively. As proved by the Raman semi-quantification data extrapolated from the analysis of MLS3, the proposed chemometric model provides solid results when it comes to the analysis of feldspar-pyroxene-olivine mixtures having a concentration ratio similar to basaltic Martian rocks analyzed in previous NASA missions. However, as displayed in Fig. 7, MLS samples also encompass a wider variety of concentration ratios. These samples serve to test the reliability of the chemometric model for the potential analysis of different igneous rocks, as is the case of the olivine-rich unit detected from orbit at the margin of Oxia Planum's landing ellipse (Mandon et al., 2019), or the feldspar-poor basaltic Martian meteorites analyzed in previous works (e.g. shergottites of lherzolitic variety (Hu et al., 2011; Borg et al., 2002)).

4. Conclusions

As shown in section 3.1, the RLS ExoMars Simulator was able to detect several fingerprint signals of medium-strong intensity from each analyzed feldspar, pyroxene and olivine phase. Considering the employed Raman system has been assembled to be qualitatively comparable to the RLS flight model, the described spectral features could be potentially used for a proper discrimination of igneous mineral phases on Mars. Knowing the position and intensity of olivine peaks vary according to the elemental composition of the sample, the RLS science team is working in the development of a dedicated multivariate method to estimate the Mg/Fe ratio within the forsterite-fayalite solid solution. However, considering that 1) similar variations were detected by the RLS ExoMars simulator in further solid solutions from feldspar and pyroxene groups, and 2) the detected signals have been used in previous works to extrapolate refined geochemical data, the results here obtained opens new perspective towards the development of additional analytical tools that could be used for a more detailed characterization of Martian mineralogy.

In this sense, the RLS science team found external calibration curves to be an extremely promising approach to maximize the scientific outcome of RLS spectra. As shown in section 3.2, from the chemometric analysis of RLS ExoMars Simulator datasets gathered from OP, OF and FP binary mixtures, calibration curves with correlation coefficients between 0.9942 and 0.9997 were obtained. Most important, the present work proves that, using binary calibration curves, ternary concentration ratios can be extrapolated.

In light of the forthcoming ESA mission to Mars this work suggests that, though the development (and further optimization) of dedicated chemometric models, the RLS spectrometer onboard the *Rosalind Franklin* rover could be potentially used to semi-quantify the main mineral components of unaltered basaltic rocks. In detail, the semi-quantification model here proposed can find application in the analysis of igneous geological units found at Oxia Planum. As detailed in the introduction section, these units have been pointed out as potential analytical targets for the ExoMars mission, as they could help deepening the current knowledge about the thermochemical evolution of Mars and its crustal formation. In this sense it is important to underline that, when it comes to the Raman semi-quantitative analysis of real Martian samples, complications could arise from 1) additional minor compounds with spectral features located in the spectral regions selected for chemometric analysis, and 2) different degree of crystallinity between Martian basaltic rocks and mineral specimens used for the construction of calibration curves. In the first case, the proposed chemometric model can be optimized by taking into consideration a wider set of vibrational indicators (maximum intensity position of additional peaks from different spectroscopic regions and their intensity ratio, see Table 4) that will make it more robust against possible spectral interferences induced by additional minor compounds. On the other side, errors deriving from the analysis of mineral species of different crystallinity could be

Table 5
Binary and ternary concentration ratio extrapolated from MLS samples through the chemometric analysis of Raman datasets collected by the RLS ExoMars Simulator.

Sample ID	Binary concentration ratios				Ternary estimation			Error			Euclidian Distance
	Calibration curve	Feldspar (wt%)	Pyroxene (wt%)	Olivine (wt%)	Feldspar (wt%)	Pyroxene (wt%)	Olivine (wt%)	Feldspar (wt%)	Pyroxene (wt%)	Olivine (wt%)	
MLS1	OF	42.5 ± 3.71		57.5 ± 3.71	25.7	37.9	36.4	0.84	−3.18	0.65	3.35
	OP		51.0 ± 6.80	49.0 ± 6.80							
	FP	40.4 ± 7.57	59.6 ± 7.57								
MLS2	OF	45.34 ± 2.32		54.7 ± 2.32	37.8	11.3	50.9	−10.5	−2.11	7.03	12.8
	OP		18.1 ± 14.1	81.9 ± 14.1							
	FP	77.1 ± 5.87	22.9 ± 5.87								
MLS3	OF	75.7 ± 7.72		24.3 ± 7.72	44.4	37.8	17.8	−1.92	−5.45	3.69	6.85
	OP		67.0 ± 6.98	32.0 ± 6.98							
	FP	54.0 ± 6.14	46.0 ± 6.14								
MLS4	OF	30.0 ± 5.90		70.0 ± 5.90	11.4	53.9	34.7	−1.09	−8.03	0.39	8.11
	OP		60.8 ± 4.96	39.2 ± 4.96							
	FP	17.5 ± 3.66	82.5 ± 3.66								
MLS5	OF	57.3 ± 6.51		42.7 ± 6.51	48.2	14.4	37.4	−3.03	−2.74	4.31	5.94
	OP		27.73 ± 10.94	72.3 ± 19.94							
	FP	77.1 ± 5.50	22.9 ± 5.50								

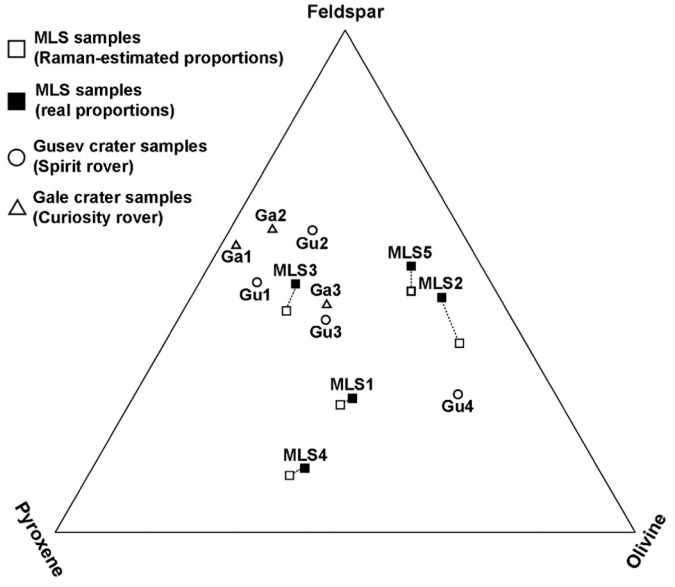

Fig. 7. Ternary diagram displaying real and calculated phase proportion of MLS samples. As reference, feldspar-pyroxene-olivine ratio of Martian basaltic rocks and soils measured by Spirit and Curiosity rovers are also provided.

minimized by analyzing additional spectral parameters of the mentioned peaks (e.g. area, symmetry and FWHM).

These variables could help to correctly identify the mineral phases composing Martian samples. As such, mineral identification could serve to elaborate correlation coefficients to better adapt external calibration curves to the samples under study. To this aim, a software for the automatic identification of mineral phases is under development and its characteristics and performances will be detailed in a dedicated manuscript. As described in section 3.4, further improvements must be also carried out to adapt the proposed model to the study of real Martian samples. However, these aspects will be addressed in a dedicated work that is under development. In light of all the above, this work summarizes the latest advances and future perspectives of the RLS Science team in the development of the chemometric tools necessary to perform semi-quantitative Raman studies on Mars, which will remarkably increase the scientific repercussion the RLS will have in the fulfilment of ExoMars mission's objectives.

Declaration of Competing Interest

None.

Acknowledgements

This work is financed through the European Research Council in the H2020- COMPET-2015 programme (grant 687302) and the Ministry of Economy and Competitiveness (Ministry of Economy and Competitiveness MINECO, grant PID2019-107442RB-C31). The authors gratefully acknowledge the support of the SIGUE-Mars Consortium (Ministry of Economy and Competitiveness MINECO, grant RDE2018-102600-T).

Appendix A. Supplementary data

Supplementary data to this article can be found online at https://doi.org/10.1016/j.icarus.2021.114542.

References

Allan, A.S.Y., Treiman, H., Bish, David L., Vaniman, David T., Chipera, Steve J., Blake, David F., Ming, Doug W., Morris, Richard V., Bristow, Thomas F.,

Morrison, Shaunna M., Baker, Michael B., Rampe, Elizabeth B., Downs, Robert T., Filiberto, Justin, Glazner, Allen F., Ralf, G., 2016. J. Geophys. Res. Planets 121, 75.
Baratoux, D., Toplis, M.J., Monnereau, M., Sautter, V., 2013. J. Geophys. Res. E Planets 118, 59.
Bendel, V., Schmidt, B.C., 2008. Eur. J. Mineral. 20, 1055.
Bibring, J.P., Hamm, V., Pilorget, C., Vago, J.L., Team, M., 2017. Astrobiology 17, 621.
Borg, L.E., Nyquist, L.E., Wiesmann, H., Reese, Y., 2002. Geochim. Cosmochim. Acta 66, 2037.
Breuer, D., Moore, W.B., 2015. Dynamics and thermal history of the terrestrial planets, the moon, and Io. Elsevier B.V. 10.
Buzatu, A., Buzgar, N., 2010. Geologie 56, 107.
Carter, J., Quantin, C., Thollot, P., Loizeau, D., Ody, A., Lozach, L., 2016. 47th lunar planet. Sci. Conf. 2064.
Chopelas, A., 1991. Am. Mineral. 76, 1101.
Devarajan, V., Funck, E., 1975. J. Chem. Phys. 62, 3406.
Ehlmann, B.L., Edwards, C.S., 2014. Annu. Rev. Earth Planet. Sci. 42, 291.
Ferdous, J., Brandon, A.D., Peslier, A.H., Pirotte, Z., 2017. Geochim. Cosmochim. Acta 211, 280.
Fornaro, T., Steele, A., Brucato, J.R., 2018a. Life 8, 1.
Fornaro, T., Boosman, A., Brucato, J.R., ten Kate, I.L., Siljeström, S., Poggiali, G., Steele, A., Hazen, R.M., 2018b. Icarus 313, 38.
Freeman, J.J., Wang, A., Kuebler, K.E., Jolliff, B.L., Haskin, L.A., 2008. Can. Mineral. 46, 1477.
Grott, M., Baratoux, D., Hauber, E., Sautter, V., Mustard, J., Gasnault, O., Ruff, S.W., Karato, S.I., Debaille, V., Knapmeyer, M., Sohl, F., Van Hoolst, T., Breuer, D., Morschhauser, A., Toplis, M.J., 2013. Space Sci. Rev. 174, 49.
Hamilton, V.E., Christensen, P.R., McSween, H.Y., Bandfield, J.L., 2003. Meteorit. Planet. Sci. 38, 871.
Hu, S., Feng, L., Lin, Y.T., 2011. Chin. Sci. Bull. 56, 1579.
Huang, Z.H., Gandais, M., 1985. Bull. Mineral. 108, 829.
Huang, E., Chen, C.H., Huang, T., Lin, E.H., Xu, J.A., 2000. Am. Mineral. 85, 473.
Ishibashi, H., Arakawa, M., Ohi, S., Yamamoto, J., Miyake, A., Kag, H., 2008. J. Raman Spectrosc. 39, 1653.
Ishibashi, H., Arakawa, M., Yamamoto, J., Kagi, H., Raman, J., 2012. Spectrosc. 43, 331.
Kabekkodu, S.N., Faber, J., Fawcett, T., 2002. Acta Crystallogr. Sect. B Struct. Sci. 58, 333.
Kizovski, T.V., Tait, K.T., Di Cecco, V.E., White, L.F., Moser, D.E., 2019. Meteorit. Planet. Sci. 54, 768.
Koeppen, W.C., Hamilton, V.E., 2008. J. Geophys. Res. E Planets 113, 1.
Kolesov, B.A., Geiger, C.A., 2004. Phys. Chem. Miner. 31, 142.
Kuebler, K.E., Jolliff, B.L., Wang, A., Haskin, L.A., 2006. Geochim. Cosmochim. Acta 70, 6201.
Lafuente, B., Downs, R.T., Yang, H., Stone, N., 2015. Highlights in Mineralogical Crystallography, 1st edn. De Gruyter, Berlin, pp. 1–30.
Lopez-Reyes, G., Rull Pérez, F., 2017. J. Raman Spectrosc. 48, 1654.
Lopez-Reyes, G., Rull, F., Venegas, G., Westall, F., Foucher, F., Bost, N., Sanz, A., Catalá-Espí, A., Vegas, A., Hermosilla, I., Sansano, A., Medina, J., 2013. Eur. J. Mineral. 25, 721.
Lopez-Reyes, G., Saiz, J., Guzmán, Á., Moral, A., Pérez, C., Rull, F., Manrique, J.A., 2018. European Planetary Science Congress 2018, vol. 12, pp. 1–2.
Mari, N., Verrino, M., 2016. EGU General Assembly, 18, p. 2016.
Martin, J.D., 2004. Using XPowder: A Software Package for Powder X-Ray Diffraction Analysis. Granada.
McSween, H.Y., Eisenhour, D.D., Taylor, L.A., Wadhwa, M., Crozaz, G., 1996. Geochim. Cosmochim. Acta 60, 4563.
Milam, K.A., McSween, H.Y., Moersch, J., Christensen, P.R., 2010. J. Geophys. Res. E Planets 115, 1.
Moral, A.G., Rull, F., Maurice, S., Hutchinson, I.B., Canora, C.P., Seoane, L., López-Reyes, G., Rodriguez Prieto, J.A., Rodríguez, P., Ramos, G., Parot, Y., Forni, O., 2019. J. Raman Spectrosc. 1.
Morschhauser, A., Grott, M., Breuer, D., 2011. Icarus 212, 541.
Mouri, T., Enami, M., 2008. J. Mineral. Petrol. Sci. 103, 100.
Mustard, J.F., Poulet, F., Gendrin, A., Bibring, J.P., Langevin, Y., Gondet, B., Mangold, N., Bellucci, G., Altieri, F., 2005. Science (80-.) 307, 1594.
Pajola, M., Rossato, S., Baratti, E., Pozzobon, R., Quantin, C., Carter, J., Thollot, P., 2017. Icarus 296, 1339.
Poulet, F., Mangold, N., Platevoet, B., Bardintzeff, J.M., Sautter, V., Mustard, J.F., Bibring, J.P., Pinet, P., Langevin, Y., Gondet, B., Aléon-Toppani, A., 2009. Icarus 201, 84.
Quantin, C., Carter, J., Thollot, P., Broyer, J., Lozach, L., Davis, J., Grindrod, P., Pajola, M., Baratti, E., Rossato, S., Allemand, P., Bultel, B., Leyrat, C., Fernando, J., Ody, A., 2016. 47th lunar planet. Sci. Conf. 2863.
Quantin-Nataf, C., Carter, J., Mandon, L., Balme, M., Fawdon, P., Davis, J., Thollot, P., Dehouck, E., Pan, L., Volat, M., Millot, C., Breton, S., Loizeau, D., Vago, J., 2019. Ninth International Conference on Mars 2019, 6317.
Mandon, L., Parkes, A.B., Quantin-Nataf, C., Bridges, J.C., Carter, J., Pan, L., 2019. Ninth International Conference on Mars 2019, 6173.
Quantin-Nataf, C., Carter, J., Thollot, P., Loizeau, D., Davis, J., Grindrod, P., Iozach, L., 2017. Geophysical Research Abstracts 19, 10163.
Riu, L., Poulet, F., Bibring, J.P., Gondet, B., 2019. Icarus 322, 31.
Rogers, A.D., Christensen, P.R., 2007. J. Geophys. Res. E Planets 112, 1.
Rull, F., Maurice, S., Hutchinson, I., Moral, A., Perez, C., Diaz, C., Colombo, M., Belenguer, T., Lopez-Reyes, G., Sansano, A., Forni, O., Parot, Y., Striebig, N., Woodward, S., Howe, C., Tarcea, N., Rodriguez, P., Seoane, L., Santiago, A., Rodriguez-Prieto, J.A., Medina, J., Gallego, P., Canchal, R., Santamaría, P., Ramos, G., Vago, J.L., 2017. Astrobiology 17, 1–28. https://doi.org/10.1089/ast.2016.1567.
Sanz-Arranz, A., Manrique-Martinez, J.A., Medina-Garcia, J., Rull-Perez, F., 2017. J. Raman Spectrosc. 48, 1644.
Sefton-Nash, P.F.E., Balme, M., Quantin-Nataf, C., Volat, J.L.V.M., Hauber, E., Orgel, C., Ruesch, O., Frigeri, A., 2020. 51st Lunar and Planetary Science Conference, p. 2417.
Servoin, J.L., Piriou, B., 1973. Phys. Status Solidi 55, 677.
Torre-Fdez, I., Aramendia, J., Gomez-Nubla, L., Castro, K., Madariaga, J.M., 2017. J. Raman Spectrosc. 48, 1536.
Treiman, A.H., 2005. Chem. Erde 65, 203.
Vago, J.L., Westall, F., Coates, A.J., Jaumann, R., Korablev, O., Ciarletti, V., Mitrofanov, I., Josset, J.L., De Sanctis, M.C., Bibring, J.P., Rull, F., Goesmann, F., Steininger, H., Goetz, W., Brinckerhoff, W., Szopa, C., Raulin, F., Edwards, H.G.M., Whyte, L.G., Fairén, A.G., Bridges, J., Hauber, E., Ori, G.G., Werner, S., Loizeau, D., Kuzmin, R.O., Williams, R.M.E., Flahaut, J., Forget, F., Rodionov, D., Svedhem, H., Sefton-Nash, E., Kminek, G., Lorenzoni, L., Joudrier, L., Mikhailov, V., Zashchirinskiy, A., Alexashkin, S., Calantropio, F., Merlo, A., Poulakis, P., Witasse, O., Bayle, O., Bayón, S., Meierhenrich, U., Carter, J., García-Ruiz, J.M., Baglioni, P., Haldemann, A., Ball, A.J., Debus, A., Lindner, R., Haessig, F., Monteiro, D., Trautner, R., Voland, C., Rebeyre, P., Goulty, D., Didot, F., Durrant, S., Zekri, E., Koschny, D., Toni, A., Visentin, G., Zwick, M., Van Winnendael, M., Azkarate, M., Carreau, C., 2017. Astrobiology 17, 471.
Vago, J.L., Coates, A.J., Jaumann, R., Korablev, O., Ciarletti, V., Mitrofanov, I., Josset, J.-L., Westall, F., De Sanctis, M.C., Bibring, J.-P., Rull, F., Goesmann, F., Brinckerhoff, W., Raulin, F., Sefton-Nash, E., Svedhem, H., Kminek, G., Rodionov, D., Baglioni, P., The ExoMars Team, 2018. Searching for Traces of Life With the ExoMars Rover, 1 st. Amsterdam, Elsevier Inc.
Veneranda, M., Manrique-Martinez, J.A., Lopez-Reyes, G., Medina, J., Torre-Fdez, I., Castro, K., Madariaga, J.M., Lantz, C., Poulet, F., Krzesińska, A.M., Hellevang, H., Werner, S.C., Rull, F., 2019a. Spectrochim. Acta - Part A Mol. Biomol. Spectrosc. 223, 117360.
Veneranda, M., Sáiz, J., Sanz-Arranz, A., Manrique, J.A., Lopez-Reyes, G., Medina, J., Dypvik, H., Werner, S.C., Rull, F., 2019b. J. Raman Spectrosc. 1.
Veneranda, M., Lopez-Reyes, G., Manrique, J.A., Medina, J., Ruiz-Galende, P., Torre-Fdez, I., Castro, K., Lantz, C., Poulet, F., Dypvik, H., Werner, S.C., Rull, F., 2020a. Astrobiology 20, 349.
Veneranda, M., Saiz, J., Lopez-reyes, G., Manrique, J.A., Sanz, A., Garcia-prieto, C., Werner, S.C., Moral, A., Madariaga, J.M., Rull, F., 2020b. Europlanet Science Congress.
Veneranda, M., Lopez-Reyes, G., Manrique-Martinez, J.A., Sanz-Arranz, A., Lalla, E., Konstantinidis, M., Moral, A., Medina, J., Rull, F., 2020c. Sci. Rep. 10, 16954.
Veneranda, M., Lopez-Reyes, G., Sanchez, E.P., Krzesińska, A.M., Manrique-Martinez, J. A., Sanz-Arran, A., Lantz, C., Lalla, E., Moral, A., Medina, J., Poulet, F., Dypvik, H., Werner, S.C., Vago, J.L., Rull, F., 2021. Astrobiology 21, 1–16.
Wang, A., Jolliff, B.L., Haskin, L.A., Kuebler, K.E., Viskupic, K.M., 2001. Am. Mineral. 86, 790.
Warren, P.H., Greenwood, J.P., Rubin, A.E., 2004. Meteorit. Planet. Sci. 39, 137.